Control of a Nacelle Inlet Ground Vortex

Derek A. Nichols[1], Bojan Vukasinovic[2], and Ari Glezer[3]
Georgia Institute of Technology, Atlanta, GA 30332-0405

Abstract

The formation of a ground vortex at the inlet of a cylindrical nacelle operating in suction near a ground plane in the presence of crosswind is significantly delayed in wind tunnel experiments using aerodynamic bleed. It is shown that the wall-normal columnar vortex is sustained by the ingestion of boundary layer vorticity that is reoriented into a wall normal component and is ultimately ingested into the inlet. Peripheral bleed actuation of the external air stream is utilized to alter and delay the near ground flow reversal on the leeward side, which precedes the vortex initiation. It is shown that azimuthally symmetric or asymmetric bleed configurations can significantly delay the ground vortex formation, albeit at the expense of the decreased total pressure recovery. Utilization of about 21% global porosity over the upper inlet surface can delay the vortex formation to over 300% of the required dimensionless inlet momentum flux in the absence of control. Moreover, the circulation of a ground vortex that eventually forms in the presence of the asymmetric bleed actuation is reduced by nearly 40% compared to the corresponding ground vortex in the absence of actuation.

Nomenclature

D	=	inlet plane diameter
h	=	ground plane distance from inlet base
I_{max}	=	circumferential distortion index
$\dot{m}$	=	inlet mass flow rate
$\dot{m}_c$	=	inlet mass flow rate at choking
$\dot{m}^*$	=	$\dot{m}/\dot{m}_c$
p_a	=	atmospheric pressure
$\widehat{p_o}$	=	face average total pressure
$\dot{P}^*$	=	dimensionless inlet momentum flux
$\dot{P}_o^*$	=	dimensionless inlet momentum flux required to form vortex
R	=	inlet plane radius
$\bar{u}$	=	mean tunnel streamwise velocity component
U_o	=	crosswind speed
V	=	average inlet velocity
V_n	=	ground vortex centerline velocity
x	=	horizontal displacement from inlet centerline
y	=	streamwise displacement from inlet face
z	=	vertical displacement from inlet centerline
Γ	=	ground vortex circulation
θ	=	azimuthal coordinate
ρ	=	ambient air density
ϕ	=	porosity
ω	=	vorticity component

[1] Graduate Research Assistant, AIAA Member.
[2] Senior Research Engineer, AIAA Member.
[3] Professor, AIAA Fellow.

I. Background

Engine nacelles of commercial aircraft must be designed to comply with the Code of Federal Regulations (CFRs) throughout all stages of flight including ground taxi, takeoff, climb, cruise, descent, and landing. Although most of the flight duration is spent in cruise, the critical design of the nacelle must accommodate operation at lower aircraft speeds during takeoff, landing, and ground operations when the performance of the engines can be strongly impacted by crosswind that can significantly alter the air intake at the inlet (Trapp et al., 2006). At low speed, the crosswind can lead to the formation of a fuselage vortex and induce inlet flow separation (even away from the ground) and while near the surface can form a ground vortex (Figure 1) (Colehour & Farquhar, 1971; Trapp & Girardi, 2012).

Once formed, the ground vortex induces distortion within the engine fan face and can also lead to the ingestion of foreign objects into the engine. As noted by Colehour and Farquhar (1971), at the time about 50% of all engines removed from aircraft for maintenance or repair had been damaged by foreign object ingestion that was previously investigated by Klein (1953). Ground vortex formation with varying engine height above ground and engine and crosswind speeds was investigated by Rodert and Garret (1955) who suggested that the formation required a stagnation line off the ground plane. This stagnation line is formed when the inlet's capture surface reaches and subsequently interacts with the ground plane (Siervi, 1981). Johns (2002) discusses how the capture surface can change in the presence of a crosswind, headwind, or tailwind. The work of Liu et al. (1985) demonstrated a linear relationship between the ratio of the mean intake and crosswind speeds, V/U_o, for which a ground vortex first forms and the ratio of the inlet elevation above ground to its diameter, H/D. Similar findings were reported by Shin et al. (1986) for inlets of varying size and orientation, and Nakayama and Jones (1996, 1999) improved this fit further and included data for small H/D and high Mach numbers.

The earlier investigations indicated that the flow characteristics of the ground vortex vary with the three formation parameters namely, the engine height above ground, the engine speed, and the crosswind speed. These parameters were investigated by Shin et al. (1986) who measured the ground vortex circulation in wind tunnel experiments while varying V/U_o, and H/D and reported that the vortex strength, as measured by its circulation, increases with V/U_o and decreases with H/D. Brix et al. (2000) performed comprehensive wind tunnel experiments and noted that the circulation of the vortex increases by increased circulation around the inlet with U_o or by increased vortex stretching with the intake velocity V. Siervi et al. (1982) suggested that there are two competing mechanisms for the inlet vortex formation associated with the variation of circulation along the nacelle by the crosswind or with the ingestion of the ground boundary layer vorticity. In experiments to investigate the former, two inlets were placed on top of one another in the absence of a ground plane. The authors reported that a vortex formed between them and concluded that the surface boundary layer was not the primary source of vorticity that leads to the vortex generation. In later

Figure 1. *A ground vortex's low-pressure core visualized by condensed water vapor on a Boeing C-17 Globemaster III during reverse thrust (Lindsay, 2023).*

numerical investigations, Trapp and Girardi (2012) verified that the formation of the vortex depends on the presence of a source of vorticity in the flow field and showed that this vorticity source can come from either the ground or the outer surface of the nacelle while noting that the vorticity generated on the nacelle's surface contributes more to the ground vortex circulation than vorticity that is transported off the ground.

As a method of controlling foreign object ingestion, Klein (1957) and Golesworthy (1959) both attempted to use a blowing jet to blow away airborne particles. Klein (1959) went on to use this blow-away jet to target the vortex directly by aiming the jet at the vortex's fixed stagnation point on the ground ahead of the inlet. This technology was utilized on a DC-8 aircraft; however, the blow-away jet itself was responsible for blowing debris off the ground and into the engine's capture envelope which meant that it produced no noticeable benefit when compared to engines operating in its absence (Johns, 2002). One major drawback of Klein's blow-away jet was that it could only target one fixed position. Smith (1970) improved upon this design by creating a volume of air directed towards the ground ahead of the inlet and spread outward from the inlet's centerline which allowed the control method to account for the movement of the vortex on the ground. Bigelis et al. (1971) instead directed air towards the back of the engine at a fixed location with the idea being that it creates an artificial headwind which prevents the necessary conditions for the origin of the ground vortex stagnation point. Vanfleet and Ruehr (1978) improved on this design by creating a sheet of air blown behind the inlet.

Simulations by Shmilovich and Yadlin (2006) utilized a control method similar to Klein (1959) in that a single jet was issued towards the front of the inlet. The major difference, however, is that the jet's location is variable and is able to change its yaw and pitch angle relative to the inlet centerline like that of a sprinkler system. This jet would not impinge on the ground to prevent debris kick up which was experienced in the control techniques which interact with the ground directly (Klein, 1957; Klein, 1959; Golesworthy, 1959). Computational results by Shmilovich and Yadlin (2006) have shown that, when using sprinkler actuation, the ground vortex ingestion can be completely suppressed; however, elements such as the fuselage vortex are still observed. Pulsed jets issued from the inlet lip which are also not directed at the ground have shown similar performance (Smith & Dorris III, 2000; Shmilovich & Yadlin, 2011).

The present experimental investigation builds on the earlier works of Nichols et al. (2022, 2023a, 2023b) that focused on the formation, characterization, sustainment, and scaling properties of ground vortices that are formed by the interaction between the nacelle and cross flow in close proximity to a ground plane. While the prior investigations focused on exploration of the parameter space for the appearance of ground vortices (Nichols et al., 2022) and a formation map in terms of the critical dimensionless parameters (Nichols et al., 2023a), the present work demonstrates how these critical parameters can be extended and offset by delaying the formation of the ground vortex through the use of a novel flow control technique based on peripherally-distributed bleed actuation.

II. Experimental Setup and Flow Diagnostics

The present experimental investigation is conducted in an open-return wind tunnel that was designed for studies of the flow physics of nacelles in crosswind (Figure 2a). The cross flow in the test section is driven by an axial blower through a 10:1 ratio contraction and the flow uniformity in the empty test section is within 1% (Nichols et al., 2023c). The axisymmetric nacelle model has an inlet plane diameter $D = 19.4$ cm (with a centerbody of diameter $0.27D$) and is mounted on an axisymmetric duct that is driven in suction by a blower where the exhaust air is released into the
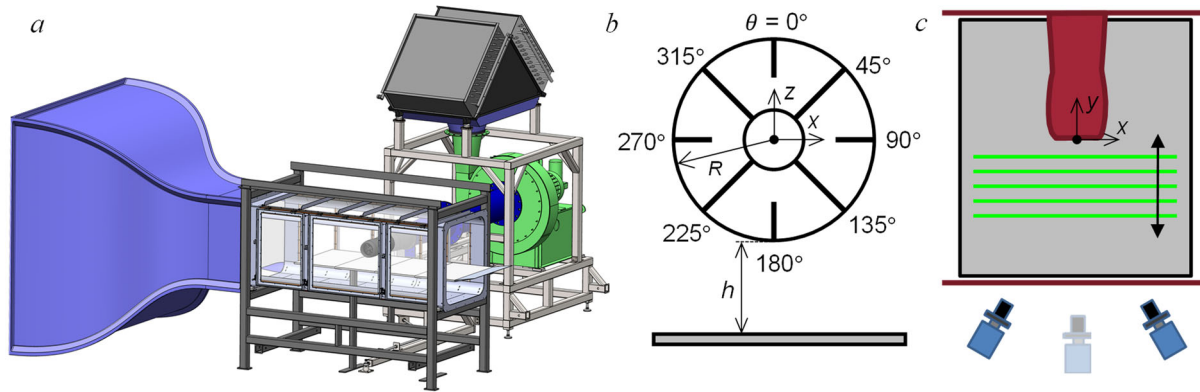
Figure 2. *a) The crosswind wind tunnel facility with the installed axisymmetric inlet and the vertically-adjustable ground plane; b) Schematic front view of the nacelle's inlet above the ground plane showing the centerbody and the rake angle θ; and c) Top view of the PIV setup, CCD camera(s') orientation and an illustration of the measurement plane(s) parallel to the inlet face.*

space through chilled water heat exchangers such that the ambient air temperature is maintained to within 1°C. The nacelle blower is driven at a prescribed mass flow rate $\dot{m}$ that is monitored using an averaging pitot probe assembly within a calibrated straight pipe segment upstream of the blower's inlet. The entire nacelle blower assembly is mounted on a moveable cart that enables axial and lateral adjustments of the nacelle's protrusion within the wind tunnel's test section (cross section 106 × 106 cm and 305 cm long, Figure 2a). In the present investigation, the nacelle model is oriented normal to the cross flow and extends through half the width of the test section. The bottom surface of the wind tunnel's test section is formed by a motorized, vertically-adjustable (to within 0.25 mm) ground plane that can be lowered down to $h = 1.45D$ below the bottom edge of the nacelle.

In the present investigations, the nacelle is operated up to $M = 0.68$ at the inlet (the maximum nacelle Mach number is 0.7) and the flow within the nacelle is characterized by the mass flow ratio $\dot{m}^* = \dot{m}/\dot{m}_c$ ($\dot{m}_c = 12.4$ lb/sec is measured at choking), which is varied between 0.16 and 1 while the tunnel's cross flow speed U_o is varied between 0 and 35 kt. Pressure recovery and flow distortion within the nacelle are assessed using a total pressure rake assembly that is located $0.40D$ downstream of the nacelle's lip at the characteristic position of the fan face. The assembly consists of 8 radial rakes that are equally distributed azimuthally (45°) with $\theta = 0°$ at the top of the inlet and increasing clockwise while alternating between 8 and 10 total pressure probes each, as shown in Figure 2b, with a higher density of probes closer to the wall. The rake total pressures are measured with a dedicated 96-channel pressure scanner with an uncertainty better than 1% of the time-averaged sample. The velocity field surrounding the nacelle is extracted from planar and stereo particle image velocimetry (PIV) in planes that are parallel to the inlet's face as illustrated schematically in Figure 2c. The PIV cameras and laser optics are placed on computer-controlled traverses that enable data acquisition in multiple planes.

III. Formation of the Ground Vortex

As shown by earlier investigators, the complex interaction of an inlet in a crosswind in close proximity to the ground surface during takeoff, landing, and ground roll can lead to the formation of a ground vortex (e.g., Colehour & Farquhar, 1971). Figure 3a shows an example image of the vertical cross section of a ground vortex captured in the wind tunnel (corresponding to Figure 2c) when the crosswind flow in the test section (from left to right) is seeded with theatrical fog and

illuminated by a laser sheet. Owing to the inlet speed and the angular velocity, the concentration of the seed particles within the vortex core is evidently lower, but because of the lower pressure within the core, it is marked by a ring of condensed water vapor. This core is visible even without the seeding particles at relatively low ambient dew point pressures as previously shown in full scale engines (c.f. Figure 1) in addition to the present investigations (Figure 3b).
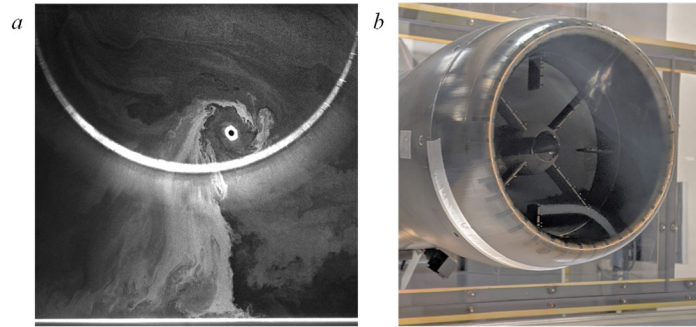

Figure 3. *a) Sectional image of the ground vortex visualized by particle seeding within a laser sheet; and b) core of the vortex visible from condensed water vapor.*

The flow conditions that lead to the onset of ground vortices that are either advected downstream or form a nominally stationary vortex that is ingested into the nacelle were investigated by Nichols et al. (2022) who showed that the appearance of a vortex depends on three formation parameters namely, the inlet mass flow rate, crosswind speed, and distance between the nacelle and ground plane. The authors showed that these parameters can be combined into two dimensionless groups: the ratio of the inlet to cross stream momentum fluxes at which the vortex first forms, $\dot{P}_o^* = (\dot{m}V/\rho U_o^2 D^2)_o$, and the ratio of the inlet plane diameter to nacelle height above the ground plane, D/h. These two parameters can be used to mark the boundary beyond which ground vortices are formed within the flow as depicted in a formation map that is reproduced in Figure 4. As noted by Nichols et al. (2023a), the use of the momentum flux ratio rather than the ratio of the inlet and crosswind speeds that implicitly excludes density variations (e.g., Nakayama & Jones, 1996, Liu et al., 1985 and Shin et al., 1986) may better convey the asymptotic behavior towards the vanishing and infinite distances of h. The data in Figure 4 show that, at any given nacelle D/h, there is a critical $\dot{P}_o^*$ above which a vortex is formed which is independent of the crosswind speed. The limit, as (D/h) decreases, indicates that the inlet momentum flux (or en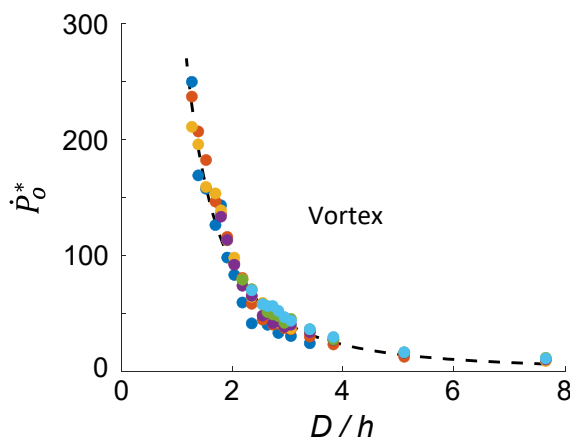gine thrust) must increase sharply to form a ground vortex when the nacelle height above the ground plane increases, indicating that a ground vortex eventually becomes unattainable. As (D/h) increases or the nacelle distance decreases, the inlet momentum flux (or engine thrust) needed for vortex formation decreases and asymptotically approaches a small but finite thrust indicating that a ground vortex can form even at vanishingly small h and a very low engine thrust. The data in Figure 4 show that the boundary for the formation of ground vortices can be represented by $\dot{P}_o^* = 375(h/D)^2$ (shown in dashed) where any value of $\dot{P}^*$ above this critical value for a given h/D will form a ground vortex.

Figure 4. *Formation boundary of the ground vortex for crosswind speeds of U_o = 10 (●), 15 (●), 20 (●), 25 (●), 30 (●), and 35 knots (●).*

5

When considering the impact within the inlet, two important metrics to consider are the total pressure recovery which is a measure of the overall loses at the fan face, and the total pressure distortion which is a measure of the nonuniformity across the fan face. A standard measure of the total pressure loss is defined as the face average total pressure $\widehat{p_o}$ (SAE International, 2017):

$$\widehat{p_o} = \frac{1}{N} \sum_i^N \widehat{p_{o,\iota}} \tag{1}$$

The ring average total pressure, $\widehat{p_{o,\iota}}$, is defined as:

$$\widehat{p_{o,\iota}} = \frac{1}{360} \int_0^{360} P(\theta)_i \, d\theta \tag{2}$$

Where $P(\theta)_i$ is the total pressure at any angle θ for a given ring i. As for the distortion, there is a range of descriptors, and the present work utilizes the circumferential distortion index, I (Colin et al., 2007), which characterizes the circumferential heterogeneity of the total pressure distributions over the fixed radii, by examining the departures between each averaged total pressure and the minimum one along the full turn at the radius:

$$I = MAX_{i=1}^{nradius-1} \left(0.5 \left[\frac{(\overline{P_i} - P_{min,i})}{\overline{P}} + \frac{(\overline{P_{i+1}} - P_{min,i+1})}{\overline{P}} \right] \right) \tag{3}$$

$\overline{P}$ is defined as the average pressure and P_{min} is the minimum pressure of the i-th crown. Finally, the maximum I value over all the considered radii for any given condition yields the maximum distortion parameter I_{max} that is used as the characteristic distortion parameter.

For each data point in Figure 4, the total pressure recovery and distortion can be calculated to evaluate the base flow just before the onset of a stable ground vortex (Figure 5), where these points are differentiated between those with and without separation on the inlet's inner windward side (denoted by dashed and solid lines, respectively). There is a clear negative, nonlinear relationship for the recovery in the absence of separation which starts at minimal values at low flow rates, while the losses grow exponentially with the inlet flow rate, eventually reaching recovery values near
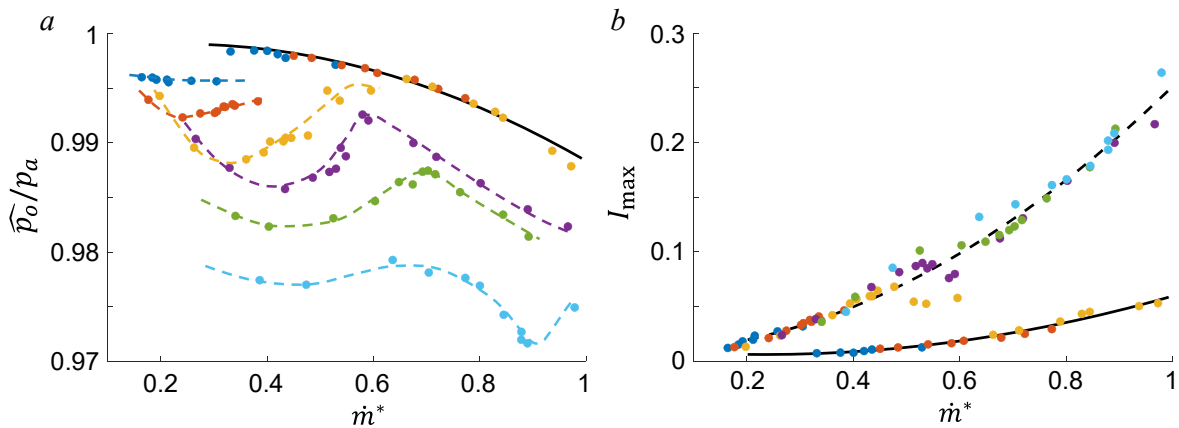

Figure 5. *a) Total pressure recovery and b) total pressure distortion immediately before the onset of the ground vortex formation for a range of inlet mass flow rates and U_o = 10 (●), 15 (●), 20 (●), 25 (●), 30 (●), and 35 knots (●) in the absence (-) and presence (- -) of internal flow separation.*

98.8% (Figure 5a). In the presence of separation, the recovery is not as well defined as evidenced by the scatter of points throughout the space dropping to recovery values of 97.1%. This scatter is attributed to the complexity of the separation bubble which can change shape, size, and position with the magnitude of the crosswind speed. As is apparent from the plot, increasing the crosswind speed increases the losses experienced for a fixed intake speed. From previous experiments, it is observed that increasing the crosswind speed will produce a separation bubble that is also of increasing size and complexity (Nichols et al., 2023c), and the losses will increase in conjunction with this bubble. Increasing the mass flow rate pulls the bubble closer to the surface while the losses within the bubble continue to increase resulting in a relationship that can rise and fall with the intake speed as per the definition of the total pressure recovery (Nichols et al., 2023c). Compared to the recovery, the distortion is much more predictable for the cases where the flow is and is not separated (Figure 5b). In the absence of separation, the average distortion can reach values of 5.3% at the highest flow rates. When the flow separates, the distortion increases with the mass flow rate independently of the crosswind speed. Because the distortion is defined as a measure of the heterogeneity of the flow, once a separation bubble is formed, it dominates the distortion magnitude such that changes in the total pressure magnitude within the separated flow have only a secondary effect on the distortion, as seen in Figure 5b. It is also interesting to note that, even though there are significant differences in the total pressure recovery and distortion between the inlet flow that is attached and separated, the ground vortex existence line shows no significant sensitivity to that difference (Figure 4). It is argued that the ground vortex formation depends on the global inlet parameters, such as its momentum flux, rather on the details of the flow about the windward lip. Furthermore, it is noted that even by changing the inlet geometry, when a drooped inlet was tested (not shown) instead of the axisymmetric geometry of the present investigation, the same critical inlet momentum flux results in the formation of the ground vortex, when keeping the other formation parameters invariant.

The structure of the flow in the vicinity of the nacelle in the absence and presence of an anchored vortex is investigated using stereo PIV in multiple cross stream planes that are normal to the ground plane and parallel to the inlet plane of the nacelle (cf. Figure 2c). The spanwise (y) spacing of these planes (along the axis of the nacelle) is equal to x-z grid spacing within each plane. These data are used to construct the 3-D time-averaged flow fields within the domain: $-1.15 \leq x/R \leq 1.64$, $0.06 \leq y/R \leq 1.56$, and $-1.82 \leq z/R \leq -0.26$. To illustrate the flow associated with the ground vortex, the 3-D flow field is illustrated using the trajectories of particles that are "seeded" near the ground plane to produce the pathlines shown in Figure 6. For $\dot{P}^* = 23$, in the absence of an anchored vortex (Figure 6a), the particles that originate near the ground plane are slightly lifted off the surface as they are advected downstream but are not carried into the inlet. As the inlet momentum flux is raised to just above the critical value to $\dot{P}^* = 42$ (Figure 6b), the intermittent formation of wall-normal vortices near the ground plane that are advected upstream is manifested by notable liftoff and turning of seeded flow upstream of the inlet that is ingested along the inlet's lower leeward side. This flow interacts with flow from underneath the inlet that is advected straight up and ingested along the lower half of the inlet face. This flow field is associated with the countercurrent flow over the ground plane that spawns the initial formation of the vortical structures as demonstrated by Nichols et al. (2023b). Finally, if the inlet momentum flux is sufficiently high, an anchored ground vortex is formed whose core is entirely seeded from flow along the ground plane where the inner core is seeded by particles that originate from directly underneath the inlet. For Figures 6c-e, it is observed that as the inlet momentum flux is increased from $\dot{P}^* = 61$ to 197, the vortex moves towards the windward side of the inlet, closer to the inlet face, and compresses in its
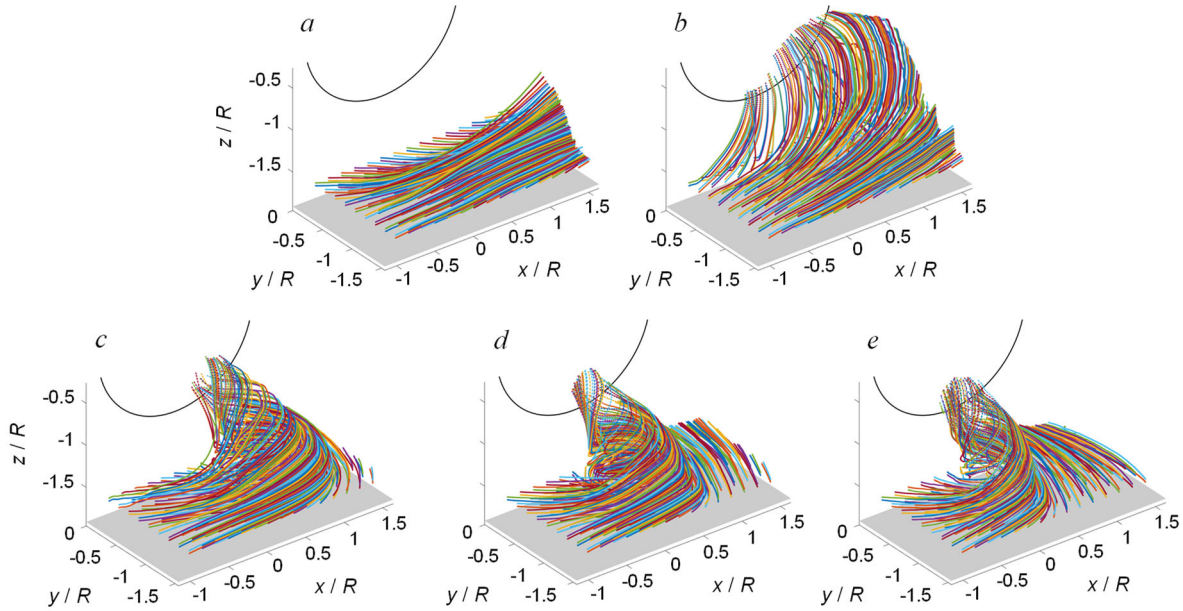
Figure 6. *Pathlines seeded from near the ground plane of the ensemble averaged volumetric flow for h/D = 0.33 and $\dot{P}^*$ = 23 (a), 42 (b), 61 (c), 82 (d), and 197 (e) with a time increment between points of $\Delta t\, U_o/D = 0.0026$.*

overall height. It is also noteworthy that, since particle positions are spaced at fixed time increments, increased spacing along the trajectories near the inlet face indicates increased local speed. The concurrent narrowing of the trajectories bundle indicates vortex stretching as it is ingested into the inlet.

As it is desired to control this vortex, it is paramount to understand how it is formed and sustained so that possible control strategies can be employed. The flow field in the presence of the anchored vortex shown in Figure 6d ($\dot{P}^*$ = 82) provides some insight into the transport of vorticity from the wall boundary layer above the ground plane along the anchored vortex. The magnitude of the spanwise and streamwise components of vorticity combine to form the vorticity component along the ground which is plotted alongside the vorticity along the vortex centerline. Since the only source of vorticity is from the wall layer, it is informative to extract the dominant vorticity domain that sustains the ground vortex (Figure 7). An isosurface of in-plane vorticity magnitude $|\omega D/U_o| = 20$ near the ground plane demonstrates the turning and liftoff of the entrained vorticity from the wall layer as the speed along the wall increases and the flow turns into the vortex. As the flow is lifted off the ground surface, the vorticity is reoriented such that the in-plane vorticity component transitions into the wall normal component. Considering the magnitude of the vorticity along the vortex centerline, as represented by the isosurface of $|\omega D/U_o| = 100$ in
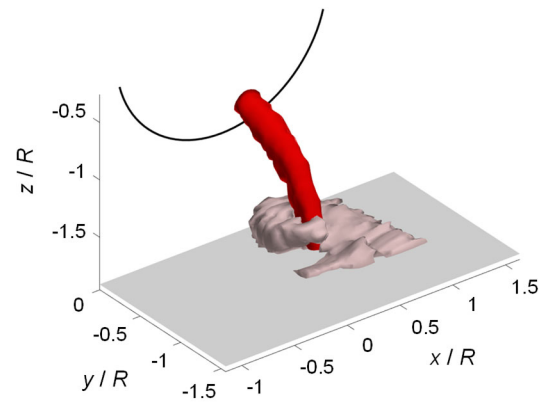

Figure 7. *Vorticity isosurfaces demonstrating the scooping of in-plane vorticity $|\omega D/U_o| = 20$ (●) out of the surface boundary layer and its reorientation into the component along the vortex centerline $|\omega D/U_o| = 100$ (●).*

8

Figure 7, the ground vortex vorticity originates from the entrainment, tilting, and stretching of the surface layer vorticity concentrations continuously entrained by the ground vortex off the ground plane boundary layer flow.

Of equal importance is understanding how to target the initial formation mechanism of the ground vortex. As shown in earlier investigations by Nichols et al. (2022), ground vortices can be engendered by a countercurrent shear layer that forms within the ground plane boundary layer as a result of interactions between the streamwise cross flow and the opposing flow induced by the suction into the nacelle. This counter current flow is created between the crosswind flow and the reversed flow induced by the suction into the nacelle once the nacelle's near wake closes on the ground plane (Nichols et al., 2023a). The process of the ground vortex initiation is shown in Figure 8 using PIV color raster plots of the time-averaged streamwise velocity which are plotted superposed with fixed-length velocity vectors within a vertical plane that is parallel and just upstream of the inlet face. Equal length vectors are used to accentuate the features embedded in the surrounding flow field which would otherwise be dominated by the inlet vectors if scaled by velocity magnitude. Contours of the inlet lip and ground surface are included for reference. At low intake speeds (Figure 8a), the flow into and around the inlet is symmetric from top to bottom. At the inlet face, flow from upstream will move around the nacelle body, wrap around, and become ingested on the leeward side. Downstream from the face, the flow forms a wake that is aligned with the crosswind direction. As the inlet momentum flux is increased, there can be a shift in the symmetry of the flow even before the formation of the ground vortex. Because the ground plane acts as an obstacle for the ingestion of flow from beneath the inlet, the inlet will instead begin to
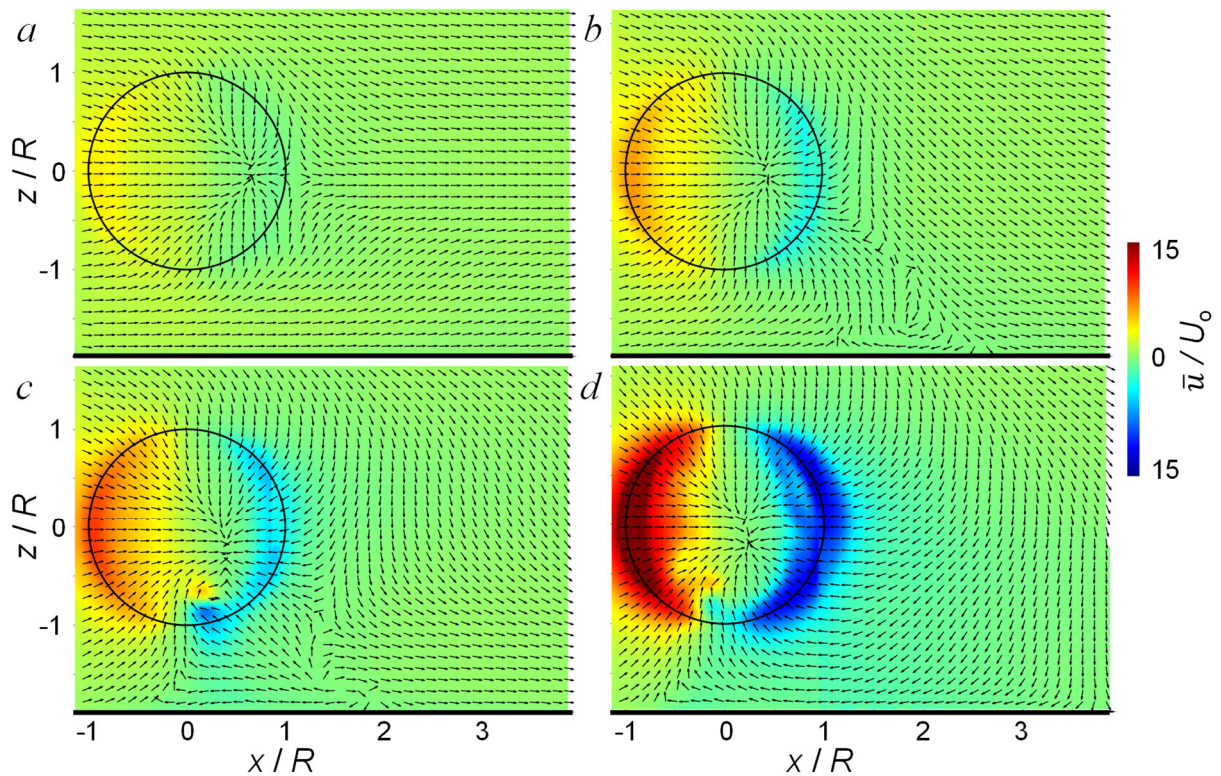

Figure 8. *Ensemble-averaged PIV color raster plots of the streamwise velocity component superposed with equal-length velocity vectors at the inlet face for $h/D = 0.33$ and $\dot{P}^* = 12.5$ (a), 35 (b), 75 (c), and 310 (d). The inlet contour and ground plane are marked for reference.*

draw additional, less resistive, flow from above. This acts to shift the saddle point of the flow on the inlet's leeward side downwards in conjunction with the initiation of the deflection of the nacelle's near wake (see Nichols et al. 2023a). Increasing the dimensionless thrust, progressively more flow is ingested from above the inlet until the nacelle's near wake deflects down to the ground plane (Figure 8b) which initiates the counter current flow at the wall as flow is drawn along the wall underneath the inlet moving against the flow of the crosswind. The further increase of the dimensionless momentum flux results in inlet flow which dominates this shear layer, therefore when a vortex forms, it moves upstream and into the inlet becoming a fully formed and ingested ground vortex (Figure 8c). Increasing the inlet flow rate even further, the vortex moves towards the windward side of the inlet as the flow from the nacelle's near wake wraps around from the top of the inlet, moves along the ground, and is ingested into the inlet (Figure 8d). As shown by Nichols et al. (2023a), the further increase in the dimensionless thrust ultimately results in the departure of the vortex through a series of complex state bifurcations.

IV. Control of Ground Vortex Formation using Distributed Bleed Actuation

The previous characterization of the nacelle flow field indicates the importance of the flow along the ground plane. The vortex initially forms because, as the flow rate of the inlet increases, the capture area of the inlet increases in tandem until it reaches the ground plane which presents an obstacle to the flow. The inlet thus begins to draw more flow
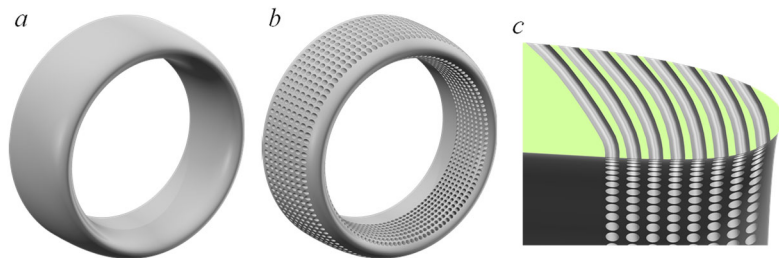

Figure 9. *CAD model of the inlet without (a) and with provision (b) for flow control, and the bleed paths over a cross section of one row streamwise row.*

from above until the near wake of the inlet closes. This event results in flow moving beneath the inlet becoming nearly stagnant and allows the inlet to more easily ingest this flow along the near-wall which ultimately results in the formation of a vortex in the ensuing shear layer. Thus, one way to prevent or delay the formation of the ground vortex is to change how the flow is ingested into the inlet. By giving the inlet more area to ingest flow around its circumference, it can delay the interaction of the flow with the ground plane which can delay the formation of the vortex. This can be achieved by using an approach originally developed to suppress internal inlet flow separation using peripheral bleed actuation (Nichols et al., 2023c). The solid, axisymmetric inlet (Figure 9a) can have an array of holes placed around its circumference which allow flow to move through the wall of the nacelle (Figure 9b). These holes are $0.021D$ in diameter and are angled such that they pull flow from behind the face (Figure 9c). As the limit case, these holes are placed around the entire circumference of the inlet in 115 equally spaced rows, each consisting of 8 holes (Figure 9b). The open area of these holes creates a maximum porosity of $\phi = 32.0\%$ compared to the total outer surface area of the inlet from the hilite to the back edge.

As a first assessment of what, if any, impact the presence of the holes imparts on the internal flow, the total pressure recovery and distortion are measured for the solid inlet and for the peripheral bleed inlet which is sealed on the outside but still having the closed holes distributed over the inner surface. An experimental testing procedure was developed to mimic the engine condition during ramp-up/down on a runway. For a given configuration, the crosswind speed and ground plane
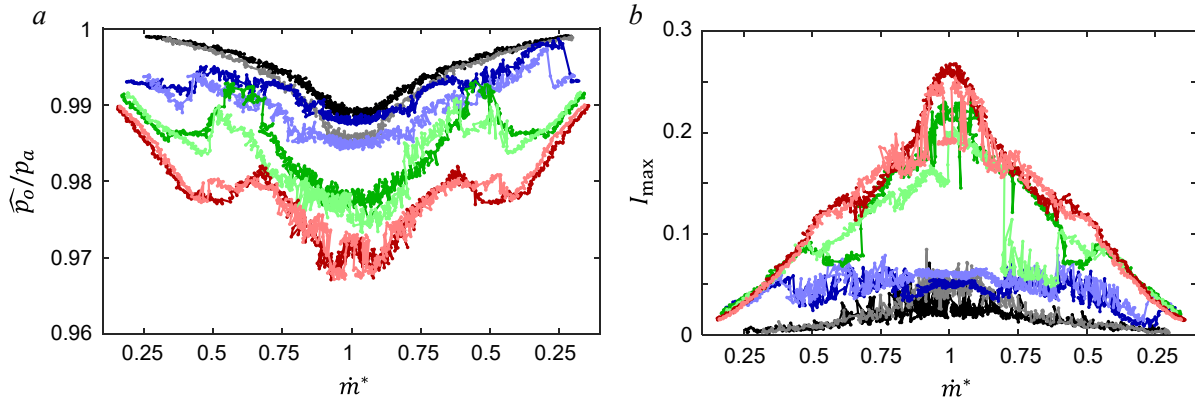
Figure 10. *Distributions of a) rake-averaged total pressure recovery and b) circumferential distortion index over a sweep of inlet mass flow rates and varying crosswind speeds of U_o = 15 (●), 25 (●), and 35 knots (●) for the solid (dark color) inlet and the sealed (light color) bleed inlet.*

distance are fixed, and the operating frequency of the blower is monotonically increased to some maximum value which results in choked flow. The inlet blower frequency is then decreased back down to the starting point at the same rate. The rate of increase and decrease was selected such that it is low enough to ensure a quasi-steady variation of the inlet flow which was verified experimentally against fixed test points. Each sweep of the inlet flow rate is done in the absence of a crosswind and in the presence of a crosswind of U_o = 15, 25, and 35 knots. Considering first the total pressure recovery in the absence of cross flow (Figure 10a), the profiles between the two inlets agree reasonably well until nearly $\dot{m}^*$ = 0.75. After this point, the sealed peripheral bleed inlet recovery starts to worsen slightly compared to the solid inlet plateauing to a level of approximately 98.6% compared to 98.9%. When a crosswind is introduced, the inlet flow is prone to separation as shown previously in work by Nichols et al. (2023c). For the case of U_o = 15 knots, the flow initially starts separated which results in decreased recovery compared to the absence of crosswind; however, a sharp increase in the recovery around $\dot{m}^*$ = 0.42 indicates that the flow attaches in this area which is also observed in Figure 5a. The solid and sealed inlets experience similar performance until approximately $\dot{m}^*$ = 0.70, after which the solid geometry slightly outperforms this modified inlet. Ultimately, the two plateau to roughly the same recovery experienced in the absence of the cross flow. For U_o = 25 knots, the flow exhibits inherent unsteadiness by attaching and reseparating multiple times with the mass flow rate sweep. This is the case for both the solid and sealed inlets, ultimately resulting in nearly identical recoveries at the maximum flow rate. Finally, for U_o = 35 knots, the performance of the two inlets is nearly identical indicating that, when separated, the losses in the flow are dominated by the flow separation which is similar between the two inlets. When the flow is attached, the roughness from the holes on the inside of the inlet can add additional losses of approximately 0.3% at the highest speeds.

The total pressure distortion, a measure of the heterogeneity of the flow, exhibits a similar trend albeit with more dramatic changes due to separation as the separation bubble poses a significant detriment to the azimuthal symmetry of the flow (Figure 10b). It is also worth noting that the profiles tend to show much better agreement in the distortion between the two inlets than what was observed in the recovery with the only major differences observed for the U_o = 25 knot crosswind while the onset of separation is unsteady and periodically changes during the sweep for the two cases. The main reason for the better agreement in the distortion is that the holes, being located

around the entire inlet, will create an axisymmetric effect around the entire inlet which does not impart a strong impact on the distortion along the azimuthal direction by the distortion parameter definition. The pressure recovery, which is a measure of the overall losses in the flow, can be affected, however, by the extra roughness on the inner surface. It is also interesting to note that, for the case of $U_o = 25$ knots, the sealed inlet exhibits improved distortion on average whereas the solid inlet performs better on nearly every other metric. This instance demonstrates the complex balance between recovery and distortion, proving that it is often a challenge to optimize both simultaneously. From the analysis of Figure 10, it is apparent that the presence of the sealed holes does not impart a strong effect on the total pressure recovery and distortion, and thus the screening of different bleed configurations is done by sealing of the unused bleed paths out of the default (full azimuthal) bleed configuration.

Initial tests examine the impact of the inlet's total porosity to assess an optimal total bleed flow for a given control effect. This is done by changing the number of open and closed rows axisymmetrically around the circumference using five percentages of the total available bleed: ϕ = 0%, 6.4%, 10.7%, 21.4%, and 32.0%, which are formed by alternating the number of open and closed rows as all closed, 1 open - 4 closed, 1 open - 2 closed, 2 open - 1 closed, and all open, respectively. Considering first the impact on the existence envelope (Figure 11a), the sealed flow control inlet experiences a nearly identical formation compared to the solid inlet; however, each of the flow control cases experiences a positive offset indicating that a larger thrust is required to form a vortex compared to identical conditions for the uncontrolled base flow. The relationship is not proportional to the porosity of the inlet, though, as the ϕ = 21.4% open inlet has the largest impact on offsetting the formation curve. ϕ = 10.7% and 32.0% perform similarly, and ϕ = 6.4% is much less effective but still improves upon the base flow. As can be expected, the total pressure losses increase with the percentage of open area where it is again noted that even the sealed inlet experiences additional losses compared to the solid inlet in the absence of separation attributed to the roughness on the inner wall from the presence of the holes (Figure 11b). When the sealed inlet does separate, it experiences a scattered offset in the recovery dependent on the crosswind speed as already demonstrated in Figure 5a. It is important to note that only the sealed inlet experiences flow separation while even the bleed inlet open only 20% prevents separation completely for these cases, as evidenced by the absence of any deviation from its recovery curve. While this control can have a large negative impact on
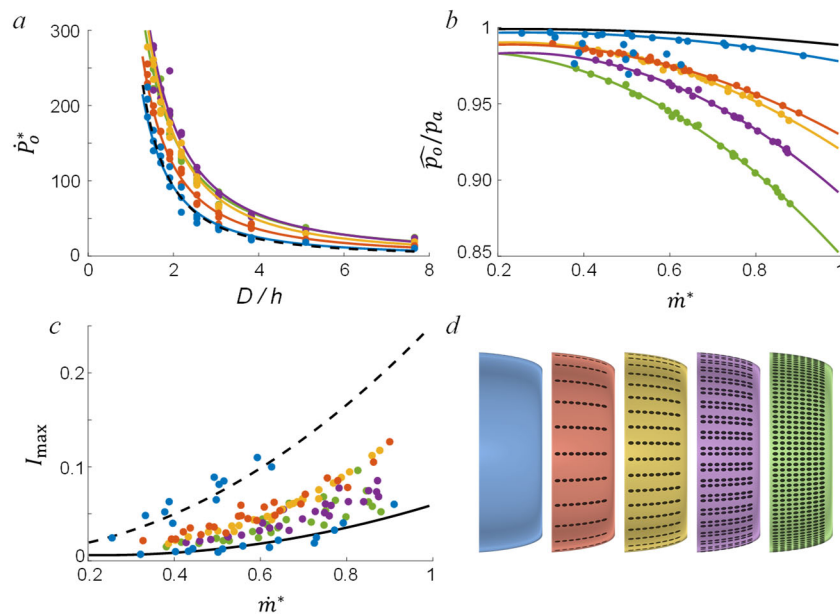

Figure 11. *Ground vortex formation envelope (a), and total pressure recovery (b) and distortion (c) for varying the global porosity of the inlet ϕ = 0% (●), 6.4% (●), 10.7% (●), 21.4% (●), and 32.0% (●) as shown schematically (d).*

the recovery, the impact on the distortion is not as extreme (Figure 11c). Because the distortion is characterized by deviations from axisymmetric flow, allowing the peripheral bleed of air around the circumference should have minimal impact on the distortion if done axisymmetrically. Included in Figure 11c are two cases for the base flow: flow in the absence of separation in solid and flow in the presence of it in dashed to use as a basis for comparison. While the sealed bleed inlet performs similarly to the solid inlet, the bleed cases all perform better than the separated base flow with the best distortion corresponding to the highest amount of bleed flow as bleeding in more flow from the periphery better enforces symmetric flow within the inlet, which is favored by the definition of the distortion parameter.

Considering these three performance metrics together, it is apparent that, by allowing the movement of air from around the circumference of the inlet, the formation of the ground vortex can be delayed to higher thrust values and that this flow can prevent separation and the large distortion signature associated with it. The tradeoff, however, is that the more air allowed to move through the wall of the inlet, the higher the total pressure losses meaning that more fuel must be burned to achieve the same flow rate. Because it is desired to delay the vortex by as much as possible, while causing the smallest impact on the recovery and distortion, the case that is chosen for further investigation is that with $\phi = 21.4\%$. In this case, there is the largest vortex formation delay, while maintaining very low levels of distortion. The only tradeoff is in the accompanying moderately high levels of total pressure losses.

As the analysis above led to the optimal global porosity of $\phi = 21.4\%$, the next step involves testing multiple axisymmetric configurations that yield approximately that global porosity, formed by alternating the number of open and closed rows as 2 open - 1 closed, 4 open - 2 closed, and 8 open - 4 closed, or by closing off the back 3 columns while keeping the front 5 open ($\phi = 20.4\%$). Interestingly, all these cases exhibit results that are remarkably similar with two exceptions (Figure 12). The ground vortex existence line is offset by nearly identical amounts for each case (Figure 12a), indicating that the effect on the external flow field is invariant of the exact orientation of the axisymmetric distribution while only depending on the total open area. The same is not true for the effect inside of the inlet, however, as the recovery and distortion are more sensitive to the distribution of the chosen flow control. For the total pressure recovery, the cases that vary azimuthally are independent of the distribution while the case
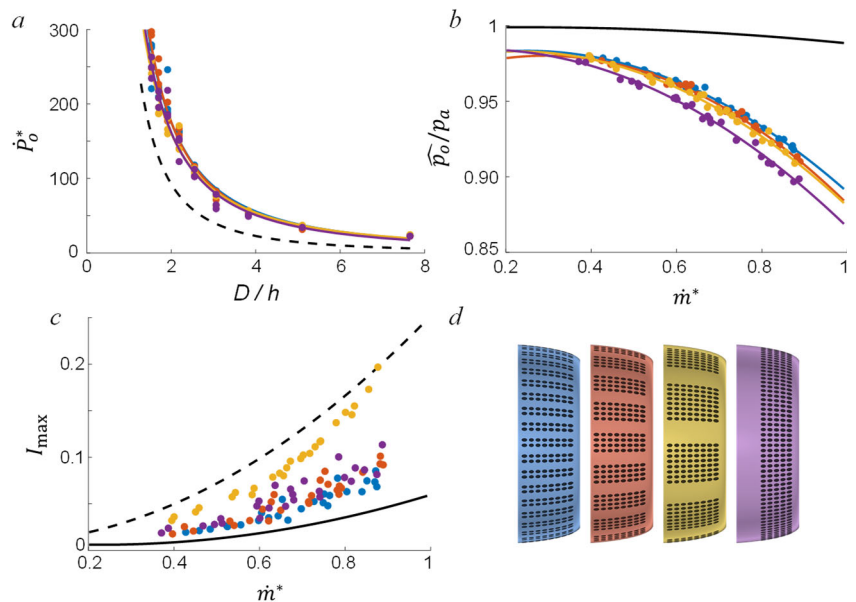

Figure 12. Ground vortex formation envelope (a), and total pressure recovery (b) and distortion (c) for the axisymmetric variation of the global porosity $\phi = 21.4\%$ by equidistant distribution of 2 (•), 4 (•), 8 (•) bleed rows, and by disabling the back 3 columns of each row (•), as shown schematically (d).

that varies in the streamwise direction induces additional losses (Figure 12b). These losses likely arise from the additional pressure drop that comes from the interaction between adjacent rows of holes. The configurations that vary azimuthally have gaps between the holes which allows the bleed effect to spread out producing less of an impact on the total pressure losses. The effect on the distortion experiences deviations for similar reasons (Figure 12c). Because the distortion benefits from axisymmetric flow, the configurations with the most uniform overall distribution experience the lowest distortion. As the gap between open holes widens, the distortion thus increases. As observed in Figure 12c, the case with the worst distortion is that which alternates 8 rows open - 4 rows closed which has flow that is the least azimuthally uniform. Generally, this analysis proves the relative independence of the ground vortex formation to the axisymmetric distribution of open bleed holes, although the impact within the inlet may vary slightly as reflected by the potential variation in the total pressure recovery and distortion measurements.

Finally, aside from axisymmetric configurations, it is possible to target or exclude specific azimuthal segments of inlet while maintaining $\phi = 21.4\%$, clearly creating an asymmetric delivery of the bleed control. This is done by closing off the bottom, windward, top, and leeward third of the bleed holes. Unlike the fully open inlet, an asymmetric distribution of openings can target the flow into specific areas of the inlet. For example, closing off the bottom holes prioritizes flow from above and away from the surface. In these cases, there are significant changes to the vortex existence line (Figure 13a). Clearly, having the bottom closed has the strongest impact on the vortex formation delay relative to the base flow. Following this case, the order of successful vortex delay descended from the leeward side, top, and windward side closed. This relationship in effectiveness has to do with what areas are preferrable to pull from in addition to which areas are not as effective. For instance, the inlet's windward side has the highest stagnation pressure and thus is the region with the strongest effect from the bleed flow while the strength of the effect diminishes up and around the inlet to its leeward side. Simultaneously, the inlet should avoid the ingestion of flow along the ground plane to further prevent the reversed flow that spawns the formation of periodic vortices in the shear layer which is why the inlet performs most optimally with the bottom holes closed. The total pressure losses and distortion for these cases all agree very well as the configurations are identical but are simply rotated around the inlet's axis and thus impart an identical effect on the internal inlet flow. It is expected that such a configuration will negatively impact the
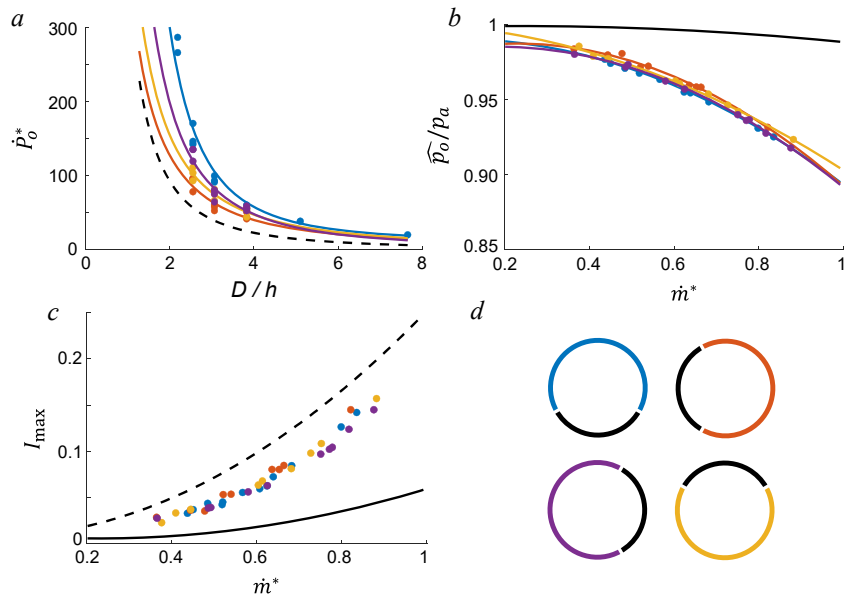

Figure 13. *Ground vortex formation envelope (a), and total pressure recovery (b) and distortion (c) for the asymmetric cumulative porosity of the inlet $\phi = 21.4\%$ by disabling the bottom (●), windward (●), upper (●), and leeward (●) section of the inlet, as illustrated schematically (d).*

distortion as it is asymmetric, and the results indicate a slightly worse distortion than the axisymmetric cases in Figures 11 and 12. Based on these results, an additional configuration was tested which combines the two best configurations – taping off the lower and leeward sides – which has a global porosity of $\phi = 13.5\%$. This data has a thrust offset that is not a strong as that with only the bottom taped, presumably because there is less flow able to be ingested from the periphery; however, it unsurprisingly has increased total pressure recovery with less open area but simultaneously worse distortion for the same reason.

V. The Effect of Controlled Bleed Actuation on the Flow Field Near the Nacelle

Further analysis of the most successful bleed-control configuration is aimed at elucidating the flow mechanisms driving the delay in the ground vortex formation. For comparison purposes, the flow field around the inlet, as well as that of the ground vortex when present, is measured for three inlet configurations at the inlet face. In addition to the most effective asymmetric bleed case (no bleed across the bottom 120° sector, Figure 13), the case with the bleed inlet fully open, which is characterized as the limit case for the bleed control, is also analyzed. Both of these controlled flow fields are compared to that of the base flow, in the absence of bleed control. The three tested flow conditions are set such that: the ground vortex does not form for any of the three inlet geometries ($\dot{P}^* = 23$), the vortex forms only in the base flow geometry ($\dot{P}^* = 82$), and the vortex forms for all three cases ($\dot{P}^* = 197$). Figure 14 presents PIV color raster plots of the time-averaged streamwise velocity which are plotted superposed with fixed-length velocity vectors within a vertical plane that is parallel and just upstream of the inlet face. A contour of the inlet lip is included for reference.

Before the vortex forms (Figure 14a-c), the flow fields all show reasonable symmetry from top to bottom. The base geometry case (Figure 14a) shows a strong velocity peak around the windward and leeward lip of the inlet reaching a magnitude of roughly $8U_o$ on the windward side. It is also interesting to note the presence of a saddle point behind the inlet that is located on the horizontal
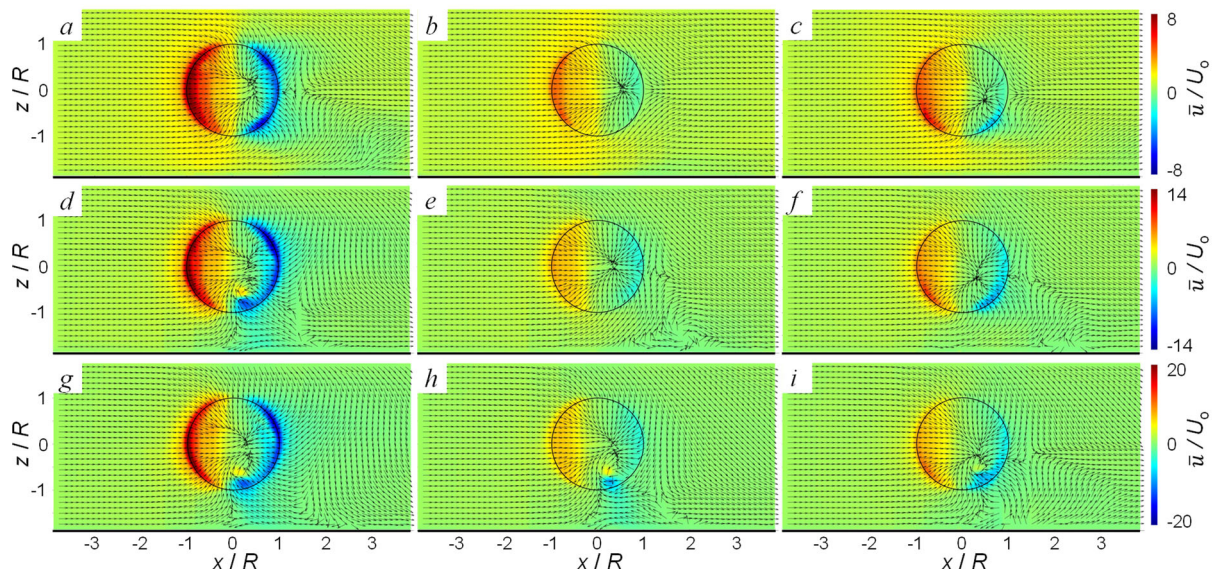

Figure 14. *Ensemble-averaged PIV color raster plots of the streamwise velocity component superposed with equal-length velocity vectors at the inlet face for a ground plane distance of h/D = 0.33 and $\dot{P}^* = 23$ (a-c), 82 (d-f), and 197 (g-i) for the uncontrolled (a,d,g), and the bleed inlet with $\phi = 32.0\%$ (b,e,h), and 21.4% with the bottom segment disabled (c,f,i). The inlet contour and ground plane are marked for reference.*

centerline. This saddle point separates the flow which moves into the inlet from above and below with the flow which simply moves around the inlet and is shed downstream, i.e., it differentiates the flow that is 'captured' by the inlet. For the case of the inlet with fully open bleed around its circumference (Figure 14b), it is interesting to note the difference in flow speeds around the lip at the face which has reduced to nearly $4.5U_o$ on the windward side. Because the inlet ingests flow through the surrounding holes, the speed at the face can be reduced while still maintaining the same inlet momentum flux as a whole. This flow field has remarkable symmetry from top to bottom with a very interesting feature showing that the saddle point in the nacelle's wake has moved towards the leeward side becoming centered on the inlet lip indicating that, unlike the base flow, no flow at the face is entering from the central leeward side of the inlet which confirms why the case of bleed centered on the leeward side showed the worst increase in performance (Figure 13). The flow also lacks the characteristic curling of flow on the upper and lower leeward sides that is typically the result of the flow being drawn from behind and into the inlet; instead that flow becomes drawn in through the bleed holes. For the case with $\phi = 21.4\%$ with the bottom segment disabled (Figure 14c), the speed of the inlet flow on the lower windward side increases relative to the fully open bleed configuration, as the flow bypassed through the bleed ports is reduced and thus the speed in that location increases in order to maintain the same inlet momentum flux. Consequently, there is a change in symmetry of the flow. The lower portion of the inlet experiences an increase in velocity more closely matching the velocity of the base flow since the bottom bleed paths are closed. This change also simultaneously displaces the sink within the inlet, the point of solely out of plane motion, downward towards the location of higher velocity further demonstrating the effect this asymmetric bleed configuration has on altering the symmetry of the flow, even internally.

When the inlet momentum flux is increased to the point of a ground vortex forming in the base flow but not for the two control cases ($\dot{P}^* = 82$), the symmetry of the flow field changes dramatically (Figure 14d). Besides the presence of the ground vortex on the lower portion of the inlet, the inlet's near wake vectors down towards the ground plane while the reversed flow along the wall underneath the inlet is an artifact of the back side of the vortex rotation. For the fully open bleed case (Figure 14e), the inlet's near wake is vectored towards the ground plane, which initiates reversed flow at the wall that is a prerequisite for the ground vortex formation (e.g. Nichols et al., 2023a). Interestingly, however, the saddle point on the leeward side of the inlet remains near the horizontal central plane during this transition which differentiates the flow topology relative to the wake vectoring for the uncontrolled case. Finally, for the case of $\phi = 21.4\%$ with the bottom segment disabled, while there is even a stagnation point on the ground formed by the closed wake, the reversed flow along the wall is still not observed. In addition, compared to the fully open bleed case, the flow along the wall beneath the inlet in this asymmetric case is able to penetrate further downstream due to the reduction in the vertical velocity component since more flow is redirected through the available bleed paths while the bottom ones are blocked.

For the highest examined inlet momentum flux ($\dot{P}^* = 197$), a vortex forms for each of the three cases (Figure 14g-i). In the uncontrolled base flow (Figure 14g), the prominent difference relative to the middle inlet momentum flux is that the vortex moves slightly towards the windward side. This motion is a result of the inlet's near wake completely wrapping around the top of the inlet and becoming ingested along the lower leeward side which was discussed previously by Nichols et al. (2023a). For the case of fully open bleed (Figure 14h), the structure of the flow field looks remarkably similar to the closed inlet at $\dot{P}^* = 82$ (Figure 14d). The wake for this case is deflected

down towards the ground plane albeit closer to the inlet surface due to the lack of the upper leeward flow angularity that exists in the absence of control. Finally, the control case with the bottom bleed section closed creates a rather complex flow field when compared to the other two realizations. A vortex is formed as evidenced by the swirling of flow within the inlet, but there is an absence of a strong signature of reversed flow beneath the inlet, likely a result of the lack of a deflected wake on the leeward side of the inlet. In fact, the field retains reasonable symmetry other than the flow in the vicinity of the vortex. The reason for this retention of the symmetry is that, because the top is open, the inlet is able to ingest additional flow from behind the inlet due to the orientation of the bleed holes (c.f. Figure 9b) while the bottom can maintain a larger velocity that prevents the deflection of the inlet's near wake due to the velocity deficit at the wall. This flow underneath the inlet, however, due to the increased suction, rapidly decelerates which eventually leads to the formation of the ground vortex even in the absence of the wake deflection.

Comparing the flow underneath the inlet in greater detail for the highest inlet momentum flux ($\dot{P}^* = 197$) (Figure 14g-i), the fields can be more quantitatively compared by considering the streamwise velocity along the ground plane at $z/R = -1.7$ (Figure 15). This method shows that the reversed streamwise velocity, a requisite parameter of the vortex formation and indicative of its strength, progressively decreases for the two control cases compared to the baseflow. Interestingly, when the fully open control case is compared to the baseflow case at $\dot{P}^* = 82$ (shown in dashed) which demonstrated a significantly similar flow field in terms of the overall structure in Figure 14d and 14h, the magnitude and distribution of the velocity near the ground is nearly identical indicating that the axisymmetric bleed simply delays the interaction with the ground plane and ultimately reaches an identical state in the surrounding flow. The baseflow at $\dot{P}^* = 197$ has a similar velocity magnitude at its peak compared to the fully open inlet but is offset further downstream. This behavior has been observed in previous studies (Nichols et al., 2023a) and is indicative of a velocity deficit that continues to increase until the inlet's near wake is completely ingested into the inlet. Considering the bleed inlet with $\phi = 21.4\%$ with the bottom segment disabled, there is a rather unique behavior of the flow near the wall which exhibits a small velocity peak compared to the other two cases and a flow which quickly plateaus downstream of the vortex, a behavior which is unique to this case further demonstrating that the bleed configuration completely alters the symmetry in the flow field.
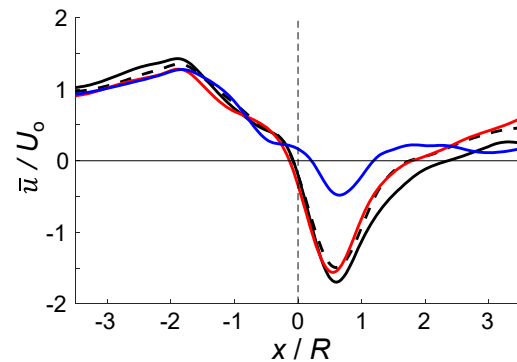

Figure 15. *Mean streamwise velocity along a horizontal elevation at $z/R = -1.70$ for $h/D = 0.33$ and $\dot{P}^* = 197$ for the uncontrolled (●), and the bleed inlet with $\phi = 32.0\%$ (●), and 21.4% with the bottom segment disabled (●). The corresponding velocity for the uncontrolled inlet at $\dot{P}^* = 82$ (--) is shown for reference.*

To complement the planar flow characterization across the inlet face, full stereo PIV measurements in successive planes across the ground vortex convey a better understanding of how the bleed control changes the full flow field about the vortex. Figure 16 plots particle pathlines for both control cases at inlet momentum flux values of $\dot{P}^* = 82$ and 197, corresponding to Figure 6d and e, respectively, for the uncontrolled base flow. For the fully open inlet at $\dot{P}^* = 82$, the inlet does, in fact, ingest flow from near the ground plane, and this flow starts to initiate the counter-current shear layer as evidenced by the non-streamlined pathlines on the lower leeward

side of the inlet. This shear layer periodically forms initial vortices that may gain strength once they ingest vorticity out of the ground boundary layer, migrate, and stretch to become ingested into the inlet (Nichols et al., 2023b). This flow field is very similar to the conditions at $\dot{P}^* = 42$ for the base flow (Figure 6b). Comparatively, the non-axisymmetric bleed distribution lacks this shear layer formation as evidenced by the smooth motion of flow near the wall while still experiencing the liftoff and ingestion of some of the approach flow near the ground plane. It is interesting to also note that the particles which form these pathlines, which
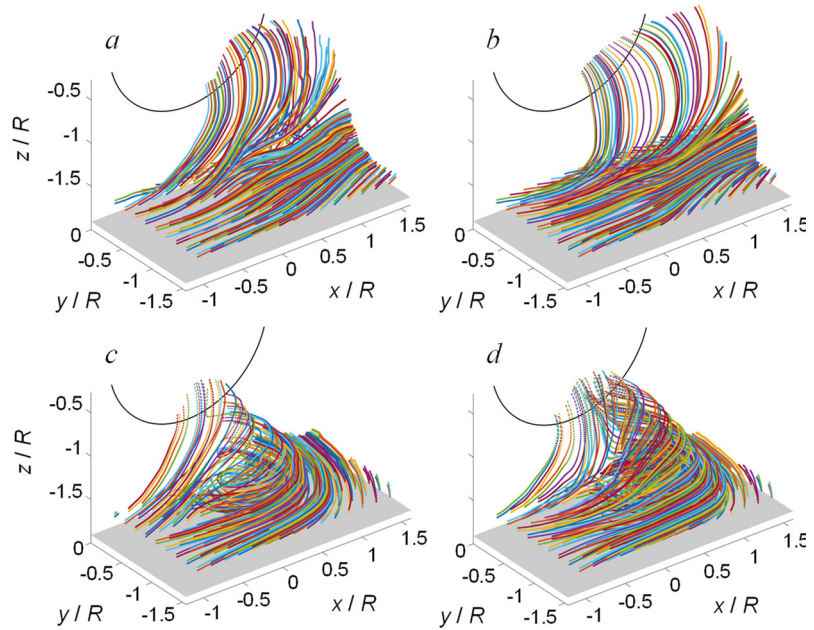

Figure 16. *Pathlines seeded from near the ground plane of the ensemble averaged volumetric flow for h/D = 0.33 and $\dot{P}^*$ = 82 (a,b), and 197 (c,d) for the bleed inlet with ϕ = 32.0% (a,c), and 21.4% with the bottom segment disabled (b,d), for a time increment between points of Δt U$_o$/D = 0.0026.*

are a fixed Δt apart, are spaced farther apart for this control case indicating that the speed at the lower half of the inlet is larger owing to the lower level of total pressure losses in the region since the holes are sealed. For the higher momentum flux case ($\dot{P}^* = 197$), a vortex does form for both control cases. For the fully open inlet, the vortex is remarkably similar to the early-stage vortex in the uncontrolled case at $\dot{P}^* = 61$ (Figure 6d) with the main exception being that flow on the lower windward side of the inlet is still ingested directly into the inlet itself instead of becoming entrained in the vortex. Comparatively, the vortex for the second control case is located further towards the leeward side. The reason for this is that the inlet is able to ingest flow at higher speeds on its lower windward side. This is evident from comparing the distance between particles for both control cases in this location. Thus, this higher momentum flow pushes the vortex farther downstream.

A more detailed comparison of these vortices can be conducted by analyzing the variation of parameters along their centerlines. The vortex center is identified using the Γ_1 criterion in each plane of the stereo PIV datasets (Graftieaux et al., 2001; Huang & Green, 2015). The center of the vortex in each plane is identified by using an area-weighted average of Γ_1 above a predetermined threshold from the 3-D data grid; this process is also repeated in horizontal planes (parallel to the ground plane). The centerline of the vortex core is computed between the ground and inlet using a second order polynomial fit through these points. Polynomial fits through the points $x(y)$ and $z(y)$ yield the streamwise and spanwise variations with height. When used together, the planar position of the vortex as a function of the distance from the ground plane is expressed using the two equations to produce a 3-D polynomial fit through the core. The three vortex centerlines for $\dot{P}^* = 197$ (h/D = 0.33) are plotted in perspective views in Figure 17a and show how the ground vortex changes for the control cases. Both the fully open bleed inlet and the inlet with the bottom
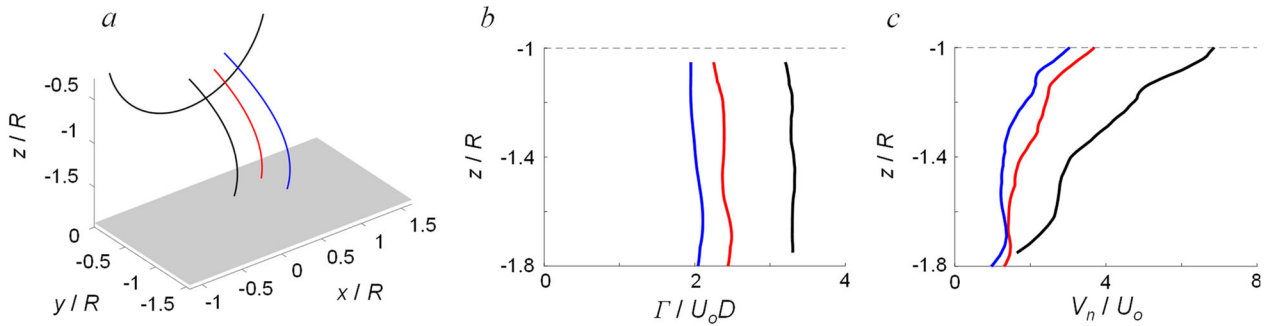
Figure 17. *a) Extracted time-averaged ground vortex centerline (a), and the vortex circulation (b) and central normal velocity (c) evolution along the centerline for h/D = 0.33 and $\dot{P}^* = 197$, for the uncontrolled (●), and the bleed inlet with ϕ = 32.0% (●), and 21.4% with the bottom segment disabled (●).*

portion closed shift the vortex further towards the leeward side while the vortex formed for the latter control is displaced further up the leeward side and further from the inlet face, both of which are features of a nominal, uncontrolled ground vortex during its early stages in development and weaker in comparison to the 'established' vortex (Nichols et al., 2023b).

Along these vortex centerlines of Figure 17a, further analysis is conducted of significant integral vortex parameters as the vortex is pulled off the surface and ingested. Of particular interest is the assessment of the variation in the vortex circulation along its centerline. For each local plane normal to the vortex centerline, the circulation is assessed within circles of increasing radii around the vortex center until the magnitude of the circulation saturates. The resulting evolution of circulation is shown in Figure 17b, which indicates a nearly-invariant circulation along the core of each vortex. Clearly, the circulation magnitude increases between cases, but for each established vortex off the ground plane, there is no significant change along its centerline suggesting that the main source of the ground vortex vorticity is indeed off the ground plane, as discussed in connection with Figure 7. What is interesting, however, is that the circulation progressively decreases from the base flow to the ϕ = 21.4% configuration, being reduced up to 38.6%. It is interesting to note that the circulation for the fully open case is very similar to the same measurement for the uncontrolled vortex which forms at $\dot{P}^* = 82$. It was previously shown that these two cases have notably similar flow fields at the inlet face (c.f. Figure 14d and h), so the similarity of the vortex circulation further indicates that the bleed around the entire inlet has an effect similar to delaying the vortex which eventually forms a similar flow field for a thrust value 2.4x higher than in the absence of the bleed control. As the flow control configuration is axisymmetric around the axisymmetric inlet, the effect of the bleed pulls additional flow from the surroundings which simply delays the interaction with the ground plane. However, the same does not hold for the second bleed configuration. Because the flow control configuration is asymmetric, it in turn produces an asymmetric effect on the flow field which is distinct throughout the further increase in the inlet flow rate and thus never mimics the baseflow unlike the fully open inlet. In addition to the circulation, the velocity along the vortex centerline can also be calculated with the 3D velocity data (Figure 17c). Near the ground, the axial velocity component of these vortices is approximately equal to the crosswind speed as the cross flow is initially lifted off the ground and into the vortex. As the vortex extends above the surface, there are three distinct regions of the evolution of its axial velocity. Close to the ground and inlet, the vortex-core velocity increases at a rate that is proportional to the inlet momentum flux, while in between these two regions, the increase in axial velocity is not as severe – at times barely increasing along the vortex centerline.

The increase in the velocity gradient closer to the inlet is attributed to the suction effect of the intake flow, which not only increases with the increase in the inlet momentum flux but also with the proximity of the vortex core to the inlet face.

VI. Conclusions

The present experimental investigations explored methods of delaying or suppressing the formation of a ground vortex in a cross flow normal to an axisymmetric nacelle near a ground plane. These investigations extend the earlier works of Nichols et al. (2022, 2023a, 2023b) that focused on mechanisms of the ground vortex formation and sustainment and established two dimensionless formation parameters within the parameter space of the ground vortex existence. The present investigations showed that, once formed, the vortex is sustained by continuous ingestion of vorticity out of the ground boundary layer. Furthermore, the ground vortex formation is independent of the details of the flow topology within the inlet, as the vortex forms at the critical dimensionless inlet momentum flux regardless of the possible presence of windward side flow separation. Because the vortex is sustained by the continuous ingestion of vorticity out of the ground boundary layer, its suppression is achieved by altering the control of vorticity transport at the ground surface. Therefore, the present flow control strategy seeks to modify the flow evolution immediately preceding the vortex formation, namely the near-ground reversed flow at the leeward side of the nacelle, *indirectly* by controlling the flow at the inlet plane. This is accomplished by peripheral aerodynamic bleed actuation through bleed paths driven by the pressure difference between the outer shell and the inner inlet surface. Thereby, by reducing the fraction of the ingested flow captured by the inlet face, the initial flow interaction with the ground surface is delayed which consequently delays a strong counter-shear near the surface that triggers the initiation of the ground vortex (as shown by Nichols et al., 2023b).

Bleed actuation was first applied using an axisymmetric distribution of azimuthally equally distributed bleed ports around the periphery of the inlet. Once its effectiveness was confirmed, consideration of different pressure domains about the inlet that drive the bleed flow into the nacelle led to additional asymmetric configurations. While each bleed configuration delays the onset of the ground vortex to a higher inlet thrust, the performance of each bleed configuration can be assessed by considering tradeoffs in the total pressure recovery and distortion.

The differences between the axisymmetric and asymmetric bleed flow configurations are documented by considering the characteristics of the ground vortex once it forms at higher dimensionless inlet momentum flux. It was shown that axisymmetric bleed patterns delay the vortex formation without significantly altering its structure, and when a vortex forms, it is remarkably similar to a vortex that forms in the absence of actuation at a lower intake flow rate. For example, with an axisymmetric porosity of 32%, the inlet momentum flux required to form a vortex can be increased to nearly 200% of the level in the absence of actuation. However, the circulation of the vortices that form in the absence and presence of actuation and the surrounding flow fields are very similar. An asymmetric bleed configuration with the bottom bleed segment closed and a porosity of 21.4%, can delay the initiation of the ground vortex to over 300% of the uncontrolled inlet momentum flux because it targets the ingestion of flow away from the ground surface. In this case, the flow field in the presence of the delayed ground vortex is markedly different from the corresponding flow in the absence of actuation, and its circulation is 40% lower. Hence, not only is the formation of the ground vortex significantly delayed, but the strength of the delayed vortex is significantly lower once formed; therefore, the risk of the ingestion of foreign objects into the engine is greatly reduced.

Acknowledgment

References

Bigelis, C. F., Colehour, J. L., Davidson, D. G., Farquhar, B. W., and Heiberg, A., "Vortex preventing method and apparatus for aircraft jet engines," U.S. Patent 3599429A, Aug. 17, 1971.

Brix, S., Neuwerth, G., and Jacob, D., "The Inlet-Vortex System of Jet Engines Operating near the Ground," AIAA Paper 2000-3998, August 2000. https://doi.org/10.2514/6.2000-3998

Colehour, J. L., and Farquhar, B. W., "Inlet Vortex," *Journal of Aircraft*, Vol. 8, No. 1, 1971, pp. 39–43. https://doi.org/10.2514/3.44224

Colin, Y., Aupoix, B., Boussuge, J. F., and Chanez, P., "Numerical Simulation and Analysis of Crosswind Inlet Flows at Low Mach Numbers," ISAIF8-0058, July 2007.

Golesworthy, G., "Tests of a blow-away jet debris guard applied to a supersonic turbo-jet intake," A.R.C. CP. No. 561, 1959.

Graftieaux, L., Michard, M. and Grosjean, N., "Combining PIV, POD and vortex identification algorithms for the study of unsteady turbulent swirling flows," *Measurement Science and Technology*, Vol. 12, No. 9, pp. 1422-1429, 2001. https://doi.org/10.1088/0957-0233/12/9/307

Huang, Y. and Green, M. A., "Detection and tracking of vortex phenomena using Lagrangian coherent structures," *Experiments in Fluids*, Vol. 56, No. 7, pp. 1-12, 2015. https://doi.org/10.1007/s00348-015-2001-z

Johns, C., "The Aircraft Engine Inlet Vortex Problem," AIAA Paper 2002-5894, October 2002. https://doi.org/10.2514/6.2002-5894

Klein, H., "Small Scale Tests on a Jet Engine Pebble Aspiration," Douglas Aircraft Co., Inc., Santa Monica Division, Publication SM 14895, 1953.

Klein, H., "An aerodynamic screen for jet engines," Douglas Aircraft Company, SM 22625, Jan. 1957.

Klein, H., "Vortex inhibitor for aircraft jet engines," U.S. Patent 2915262A, Dec. 1, 1959.

Lindsay, B., "Engine Inlet Vortices from C-17 Globemaster III," *Bill Lindsay Pixels*, 2023. https://bill-lindsay.pixels.com/featured/engine-inlet-vortices-from-c-17-globemaster-iii-bill-lindsay.html. Used with permission.

Liu, W., Greitzer, E. M., and Tan, C. S., "Surface Static Pressures in an Inlet Vortex Flow Field," *Journal of Engineering for Gas Turbines and Power*, Vol. 107, No. 2, 1985, pp. 387–393. https://doi.org/10.1115/1.3239738

Nakayama, A., and Jones, J. R., "Vortex Formulation in Inlet Flow near a Wall," AIAA Paper 96-0803, January 1996. https://doi.org/10.2514/6.1996-803

Nakayama, A., and Jones, J. R., "Correlation for Formation of Inlet Vortex," *AIAA Journal*, Vol. 37, No. 4, 1999, pp. 508–510. https://doi.org/10.2514/2.743

Nichols, D. A., Vukasinovic, B., Glezer, A., and Rafferty, B, "Formation of a Nacelle Inlet Ground Vortex in Crosswind," AIAA Paper 2022-1698, January 2022. https://doi.org/10.2514/6.2022-1698

Nichols, D. A., Vukasinovic, B., and Glezer, A., "Scaling Characteristics of Ground Vortices in a Nacelle Inlet Flow Field," AIAA Paper 2023-1981, January 2023. https://doi.org/10.2514/6.2023-1981

American Institute of Aeronautics and Astronautics

Nichols, D. A., Vukasinovic, B., and Glezer, A., "The Formation, Evolution, and Sustainment of Inlet Ground Vortices," AIAA Paper 2023-3891, June 2023. https://doi.org/10.2514/6.2023-3891

Nichols, D. A., Vukasinovic, B., Glezer, A., and Rafferty, B., "Aerodynamic control of an inlet flow in crosswind using peripheral bleed actuation," *Journal of Propulsion and Power*, Sept 2023. https://doi.org/10.2514/1.B38944

Rodert, L. A., and Garrett, F. B., "Ingestion of Foreign Objects into Turbine Engines by Vortices," NACA TN 3330, February 1955.

SAE International. SAE ARP1420C - Gas Turbine Engine Inlet Flow Distortion Guidelines. April 2017.

Shin, H. W., Greitzer, E. M., Cheng, W. K., Tan, C. S., and Shippee, C. L., "Circulation Measurements and Vortical Structure in an Inlet-Vortex Flow Field," *Journal of Fluid Mechanics*, Vol. 162, No. 8, 1986, pp. 463–487. https://doi.org/10.1017/S0022112086002124

Shmilovich, A., and Yadlin, Y., "Engine Ground Vortex Control," AIAA Paper 2006-3006, June 2006. https://doi.org/10.2514/6.2006-3006

Shmilovich, A., and Yadlin, Y., "Flow Control Techniques for Transport Aircraft," *AIAA Journal*, Vol. 49, No. 3, 2011, pp. 489–502. https://doi.org/10.2514/1.J050400

Siervi, F. D., "A Flow Visualization Study of the Inlet Vortex Phenomenon," Massachusetts Institute of Technology, Gas Turbine and Plasma Dynamics Laboratory, GT & PDL Report No. 159. 1981.

Siervi, F. D., Viguier, H. C., Greitzer, E. M., and Tan, C. S., "Mechanisms of Inlet-Vortex Formation," *Journal of Fluid Mechanics*, Vol. 124, 1982, pp. 173–207. https://doi.org/10.1017/S0022112082002456

Smith, J. P., "Protective air curtains for aircraft engine inlets," U.S. Patent 3527430A, Sep. 8, 1970.

Smith D. M. and Dorris III, J., "Aircraft engine apparatus with reduced inlet vortex," U.S. Patent 6129309A, Oct. 10, 2000.

Trapp, L. G., Argentieri, H. G., de Souza, F. J., and Girardi, R. da M., "Aspects of Isolated Nacelles Near the Ground During Crosswind Operation," ENCIT Paper CIT06-0740, December 2006.

Trapp, L. G., and Girardi, R., "Evaluation of Engine Inlet Vortices Using CFD," AIAA Paper 2012-1200, January 2012. https://doi.org/10.2514/6.2012-1200

Vanfleet, C. R. and Ruehr, W. C., "Method and apparatus for limiting ingestion of debris into the inlet of a gas turbine engine," U.S. Patent 4070827A, Jan. 31, 1978.

American Institute of Aeronautics and Astronautics